**RESEARCH PAPER**

# Microstructural evolution of 2.25Cr-1Mo-0.25V submerged-arc weld metal

Hannah Schönmaier[1] [ID] · Fred Grimm[2] · Ronny Krein[2] · Katharina Kirchheimer[1] · Ronald Schnitzer[1]

## Abstract
Heat-resistant V-modified 2.25Cr-1Mo-0.25V-weld metal is commonly used in petrochemical industry for heavy wall pressure vessels in high-temperature hydrogen service. In order to improve the reactor efficiency, the weldments have to endure even higher temperatures and pressures. Acicular ferrite (AF) is often regarded as the optimum microstructure due to its good combination of strength and toughness. As few literature about the evolution of microstructure and the final microstructure constituents of 2.25Cr-1Mo-0.25V weld metal is available, the current paper intends to provide comprehensive information by means of microscopy, crystallographic examination via electron backscatter diffraction and in situ observation of the austenite to ferrite phase transformation via high-temperature laser scanning confocal microscopy (HT-LSCM). The investigated weld metal exhibits a high density of complex aluminium-silicon-manganese oxides with a spherical shape and large prior austenite grains, which in combination is beneficial for intragranular nucleation of AF. Nonetheless, the examination of the transformed final microstructure was not sufficient to make an unambiguous statement about the presence of AF within the 2.25Cr-1Mo-0.25V weld metal. Via in-situ HT-LSCM of the phase transformation, intragranular nucleation of AF at non-metallic inclusions within the austenite grains was detected, which confirms that even though the microstructure of 2.25Cr-1Mo-0.25V weld metal is mainly bainitic, small amounts of AF are present.

**Keywords** 2.25Cr-1Mo-0.25V · Weld metal · Microstructure evolution · High-temperature laser scanning confocal microscopy · Bainite · Acicular ferrite

# 1 Introduction

## 1.1 2.25Cr-1Mo-0.25V weld metal

The heat-resistant V-modified 2.25Cr-1Mo-0.25V-alloy was developed following the conventional low-alloyed 2.25Cr-1Mo steel and approved as ASME Code Case 2098–1 in 1991 [1, 2]. 2.25Cr-1Mo-0.25V-alloy is commonly used in the petrochemical industry where it is applied to hydrocracking reactors

as well as heavy wall pressure vessels for high-temperature hydrogen service [1, 3]. Compared to the base alloy 2.25Cr-1Mo, the V-modified alloy can withstand higher stresses, which made a reduction of reactor wall thicknesses in combination with higher operating temperatures possible, thus leading to better efficiency [1, 3]. In 1995, the Italian company Nuovo Pignone was the first to fabricate a reactor from 2.25Cr-1Mo-0.25V-alloy in Europe, finally leading to the manufacturing of more than 90 further reactors by the end of 2001 [1]. This V-modified version of the 2.25Cr-1Mo steel has several advantages such as high strength at elevated temperatures and a good resistance to both hydrogen attack and overlay disbonding. Beside the listed benefits, the application of 2.25Cr-1Mo-0.25V-alloy entails some disadvantages too. These include low toughness levels in as-welded condition before post weld heat treatment and a higher susceptibility to reheat cracking compared to the conventional Cr-Mo grade [3, 4]. Regarding the application in hydrotreating reactors, 2.25Cr-1Mo-0.25V weld metal has to withstand combinations of hydrogen partial pressures up to 13.79 MPa and temperatures up to 482 °C to avoid hydrogen attack [2, 5, 6].

✉ Hannah Schönmaier
hannah.schoenmaier@unileoben.ac.at

1 Department of Materials Science, Montanuniversität Leoben, Franz-Josef-Straße 18, 8700 Leoben, Austria

2 voestalpine Böhler Welding Germany GmbH, Hafenstraße 21, 59067 Hamm, Germany

In order to further improve the reactor efficiency, petro-chemical industry demands for even higher allowable temperatures and pressures. To meet this request, detailed knowledge of the 2.25Cr-1Mo-0.25V weld metal microstructure is indispensable before adjustments to the chemical composition or post weld heat treatment can be applied. The microstructure shows significant influence on the weld metals mechanical properties such as fracture toughness and strength at ambient and increased temperatures. Depending on the type and amount of the microstructure constituents, the weld metal properties can vary to a lesser or greater extent. According to literature, it is agreed that with decreasing temperature, different transformation structures such as grain boundary primary ferrite, Widmanstätten ferrite, acicular ferrite (AF), upper bainite and lower bainite can appear in weld metals [7]. The transformation temperatures of Widmanstätten ferrite, AF and bainite lie in a similar temperature range [8].

## 1.2 Acicular ferrite formation

Intragranular AF which is typical for low-alloyed weld metal is often regarded as the optimum microstructure constituent with a good combination of strength and toughness due to its small interlocking grains and high angle boundaries. This intragranularly nucleated ferritic microstructure was first described in the early 1970s by Smith et al. [9, 10]. Farrar and Harrison stated that the optimum strength-toughness relation of Carbon-Manganese weld metal can be obtained with a microstructure which consists of more than 65% AF with a very small lath size of around 1 μm [10]. The typical chaotic interlocking lath arrangement of AF with its high angle boundaries can be attributed to its mechanism of formation [9, 11]. During the early stages of the austenite to ferrite transformation, primary AF laths nucleate heterogeneously at the interface of potent non-metallic inclusion within the austenite grains [8, 11–13]. Once these primary AF laths have nucleated, the nucleation of further small AF laths proceeds sympathetically on the interface between existing AF laths and the surrounding austenite so there is no one to one correspondence between AF and the nucleation sites. Due to the progressive reduction of remaining austenite, impingement events of AF plates take place which leads to the characteristic fine-grained interlocking microstructure [8, 11, 12]. This chaotically appearing microstructure constituent significantly enhances the toughness as its disordered laths with different crystallographic orientations cause a retardation of the propagation path for cleavage cracks compared to the ordered ferritic lath structure of bainite [14].

## 1.3 Influencing factors on acicular ferrite formation

Whether AF occurs as a microstructure constituent or not depends on several influencing factors such as the weld metal chemical composition, the cooling rate after welding, the size, composition and amount of non-metallic inclusions as well as the austenite grain size [10, 13–15].

### 1.3.1 Alloying elements

Beside the carbon content, the elements manganese, chromium and molybdenum show considerable influence on the formation of AF [10, 13–15]. Increasing levels of manganese up to 1.8 wt.% were found to reduce the amount of polygonal and side plate ferrite by increasing the amount of AF at the same time as well as depressing the austenite to ferrite transformation temperatures at almost all cooling rates [10]. Molybdenum up to 0.5 wt.% leads to an increase of the amount of AF. Higher molybdenum leads to a contrary effect [10, 15]. Chromium shows a quite similar behaviour, whereby chromium contents exceeding 1 wt.% lead to a reduction in AF as it is replaced progressively with bainite [15].

Furthermore, the oxygen level was found to have a significant impact on the amount of AF in weld metal produced by submerged-arc welding (SAW). Very high oxygen contents greater than 600 ppm entail a high inclusion density which subsequently leads to a restricted austenite grain size and the formation of ferrite side-plates, whereas oxygen contents around 300 ppm promote AF by providing sufficient oxygen for the formation of effective non-metallic inclusions for intragranular nucleation of ferrite plates. Further reduction in oxygen content combined with an increasing amount of alloying elements leads to the formation of bainite consisting of parallel ferrite laths [16, 17]. Barbaro et al. [18] state that weld metal oxygen levels in the range of 150 to 300 ppm are most beneficial for the formation of AF [18]. Furthermore, soluble elements like, e.g. boron can reduce the austenite grain boundary energy via segregation which in further consequence leads to an increase of the energy barrier for ferrite nucleation on the grain boundary surface thus promoting intragranular nucleation events [7, 14, 19–21]. Nevertheless, Lee et al. [22] described that high boron contents exceeding 32 ppm lead to a reduction of AF and an increase of upper bainite in high strength low-alloy weld metal.

### 1.3.2 Austenite grain size

It has become evident that the possibility of intragranular nucleation of AF depends directly on the ratio between the surface area of inclusion particles and the surface area of grain boundaries. With increasing austenite grain size, the fraction of AF rises [14]. As the growth of austenite grain size is limited by the inclusions present in the weld metal, an increase of austenite grain size above a certain optimum value which depends on the weld metals chemical composition and cooling rate does not lead to a higher amount of AF. Further increase of austenite grain

size then is directly accompanied by a reduced amount of inclusions needed for intragranular nucleation of AF [14, 23].

### 1.3.3 Non-metallic inclusions

Besides the austenite grain size and potentially present grain boundary segregation of Boron or allotriomorphic ferrite which forms at the prior austenite grain boundaries at the beginning of austenite to ferrite phase transformation in some weldments, non-metallic inclusions play a key role in the process of ferrite nucleation. Depending on the type and chemical composition of the non-metallic inclusion and its diameter, it can act as a nucleation surface for ferrite laths and therefore promote intragranular nucleation [7, 13–15, 24].

Lee et al. [13] have established four different types of non-metallic inclusions which affect the austenite to ferrite transformation in various ways. Figure 1 gives a modified schematic overview [13] of these inclusion types. In general, they can be divided into two sections: nucleant inclusions which promote intragranular nucleation of ferrite laths (type 3 and type 4) and non-nucleant inclusions which lie in the middle of ferrite laths (type 1) or at the boundary of two adjacent ferrite laths (type 2) and which do not support intragranular nucleation according to Lee et al. [13].

However, large inclusions are more preferential nucleation sites for AF than smaller inclusions. Furthermore, the increase of non-metallic inclusion size supports multiple nucleation events of primary AF laths with different crystallographic orientations [13]. Lee et al. found that the probability of AF nucleation strongly increases with increasing inclusion diameters in the range from 0.4 to 0.8 until it reaches a constant value for inclusions above 1.1 μm in diameter [13, 14]. Zhang et al. determined that for C-Mn-Ni weld metal with an intermediate oxygen level between 200 and 350 ppm inclusions in the size range of 0.3 to 0.9 are most favourable for AF nucleation [24].
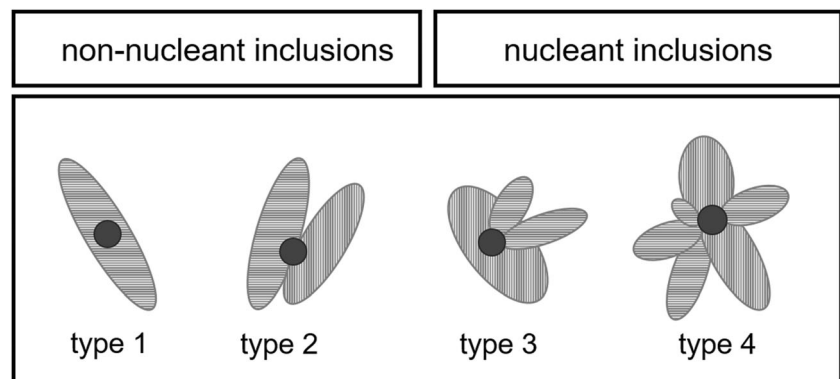
### 1.3.4 Cooling rate

Another important influencing factor on the weld metal microstructure is the cooling rate. Increasing cooling rates are known to lower the transformation temperatures leading to intragranular nucleated microstructure constituents at intermediate cooling rates on the order of 15 °C/s in a temperature range between 800 and 500 °C [10] which is suitable for the investigated SAW 2.25Cr-1Mo-0.25 weld metal. If the weld metal is boron treated, the optimal cooling rate for AF formation is also affected by the boron content and the austenite grain size [25]. Depending on the chemical composition and the cooling rate of the weld metal, the intragranular nucleation of AF laths begins at 650 to 440 °C, thus lying in the bainite range of temperatures [14].

Literature regarding low-alloyed 2.25Cr-1Mo-0.25V weld metal and steel deals a lot with challenges concerning joining, post weld heat treatment, creep damage and repair issues [3, 26–32] as well as the evolution of carbides during heat treatment [33–35]. As a result, only little precise information about the evolution of microstructure in the course of phase transformation and the final microstructure constituents is available. In most cases, the 2.25Cr-1Mo-0.25V weld metal microstructure is described as simply bainitic without discussion about the different kinds of potentially present bainitic-ferritic microstructure constituents. Regions of chaotic ferrite lath arrangement found during optical microscopy of SAW 2.25Cr-1Mo-0.25V weld metal raised questions about its actual microstructure composition as in literature intragranular nucleated AF is mostly associated with much lower alloyed steels [11, 12, 21, 36–39]. Therefore, the current paper intends to provide comprehensive information about the evolution and composition of 2.25Cr-1Mo-0.25V weld metal microstructure through investigation via microscopy, crystallographic examination via electron backscatter diffraction (EBSD) and in situ observation of the austenite to ferrite phase transformation.



**Fig. 1** Modified schematic overview of the four types of non-metallic inclusions occurring in weld metal, according to Lee et al. [13]. Type 1 and type 2 inclusions are considered non-nucleant; type 3 and type 4 are nucleant inclusions promoting AF formation [13]

## 2 Experimental procedures

### 2.1 Material investigated

The chemical composition of the 2.25Cr-1Mo-0.25V multi-layer weld metal is presented in Table 1.

Beside the listed elements, phosphorus and sulphur were also present in small amounts (< 80 ppm).

The investigated multi-layer weld metal with two weld beads per layer was produced by SAW using a weld gap of 22 mm. Figure 2 shows a macro-etched cross section of such a weldment. The position for microstructure investigation was the last weld bead which is not influenced by following weld beads, see red rectangle in Fig. 2.

The samples were manufactured by tandem-SAW with welding conditions shown in Table 2.

The weld metal was in the as-welded condition and experienced only a low hydrogen annealing (soaking at 350 °C for 4 h) to remove diffusible hydrogen in the weld seam area. This procedure is commonly applied in practice to avoid hydrogen-induced cold cracking.

### 2.2 Investigation of the microstructure

The 2.25Cr-1Mo-0.25V weld metal microstructure was observed by means of light optical microscopy (OM), scanning electron microscopy (SEM), electron backscatter diffraction (EBSD) and energy dispersive X-ray diffraction (EDX) as well as high-temperature laser scanning confocal microscopy (HT-LSCM).

For the OM investigation, the specimen was ground with SiC abrasive paper and polished with 3 μm and 1 μm diamond suspension and colour etched with 10% aqueous sodium metabisulfite which forms a thin sulphide film on the sample surface. The colouring visible during OM depends on the film thickness and, therefore varies with the local chemical composition and crystallographic orientation of the sample. For imaging, bright field contrast was chosen.

SEM and EBSD analysis were conducted in a FEI Versa 3D DualBeam workstation equipped with an EDAX Hikari XP EBSD system. For SEM and EBSD analysis, the specimens were ground with SiC abrasive paper and polished with 3 μm and 1 μm diamond suspension as well as electrolytically polished to reduce stresses resulting from plastic deformation. EBSD measurements were done using analytical mode with a step size of 0.3 μm, a working distance of 11 mm, an
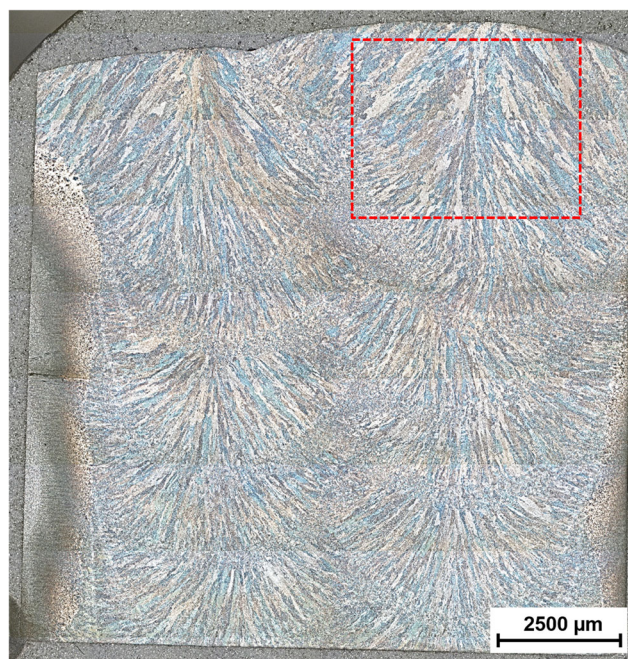


**Fig. 2** Macro-etched cross section of the investigated 2.25Cr-1Mo-0.25V SAW weld metal. The position in the last weld bead where the specimens were taken is highlighted with a red rectangle

acceleration voltage of 30 kV and 4 × 4 binning. The crystallographic information was analysed using the OIM data Analysis 8 (EDAX inc.) software. The prior austenite grains where reconstructed based on the crystallographic orientation relationship between the parent phase austenite and the daughter phase ferrite using the program ARPGE implemented by Cayron [40]. For reconstruction, the Nishiyama-Wasserman orientation relationship was used as it ensures the highest reconstruction quality according to literature [41].

EDX mappings were performed with a SEM type 7200F produced by Jeol using an in-lens schottky-fieldemitter. For the EDX measurements, the specimen surface was ground with SiC abrasive paper and polished with 3 μm and 1 μm diamond suspension. To minimize the influence of the surrounding matrix, only non-metallic inclusions ≥ 1 μm in diameter were investigated.

The HT-LSCM for the in situ observation was conducted in a laser scanning confocal microscope type VL2000DX produced by Lasertec with an attached high-temperature furnace type SVF17-SP. For this purpose, a 5 × 5 × 0.5 mm specimen was ground with SiC abrasive paper and polished with 3 μm and 1 μm diamond suspension before it was placed in an aluminium oxide crucible. The applied heating cycle is shown

| | Fe | Cr | Mn | Mo | V | Si | C |
|---|---|---|---|---|---|---|---|
| **Table 1** Chemical composition in wt.% of the investigated 2.25Cr-1Mo-0.25V SAW weld metal | Balance | 2.2–2.3 | 1.1–1.2 | 0.95–1.05 | 0.25–0.35 | 0.1–0.15 | 0.08–0.10 |
| | Cu | W | Nb | N | Al | Ti | O |
| | 0.03–0.04 | 0.005–0.01 | 0.01–0.02 | 0.01–0.02 | 0.005–0.01 | 0.001–0.003 | 0.020–0.025 |

**Table 2** Overview of tandem-SAW conditions

| Polarity | Voltage | Current | Heat input | Interpass temperature | Preheat temperature |
|---|---|---|---|---|---|
| AC/AC | 30 V | 550 A | 25 kJ/cm | 200–230 °C | 200 °C |

in Fig. 3. The sample was heated at 4 °C/s to 1400 °C for austenitization and immediately cooled at 11 °C/s afterwards. The solid line shows the adjusted and the dashed line shows the effective cooling rate which deviates from the solid line at a certain temperature.

With the help of HT-LSCM, the nucleation and growth of ferrite laths at active inclusions and grain boundaries during austenite to ferrite phase transformation can be directly observed, leading to a better understanding of the transformation behaviour of 2.25Cr-1Mo-0.25V weld metal.

# 3 Results

## 3.1 Light optical microscopy

Figure 4 shows OM pictures of the 10% aqueous sodium metabisulfite etched 2.25Cr-1Mo-0.25V weld metal at different magnifications. The ferrite laths are arranged in packets of different sizes to a large extent, see parallel arrows in Fig. 4a. In between these ordered bainitic packets of ferrite laths, regions which exhibit a far more chaotic arrangement of the laths are apparent, as in the encircled region of Fig. 4a. Figure 4b shows such an area of disordered lath arrangement at a higher magnification. Beside the irregular lath arrangement, the OM picture also shows a star-like arrangement of ferrite laths, as shown in dashed circle in Fig. 4b.
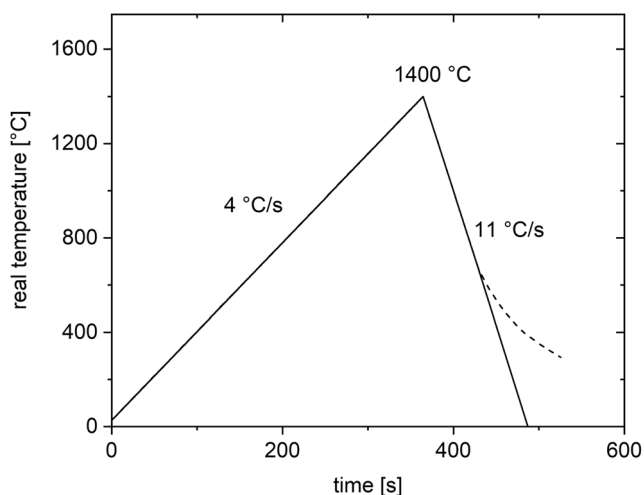


**Fig. 3** Schematic illustration of the in situ heating cycles for HT-LSCM of 2.25Cr-1Mo-0.25V weld metal. The solid line shows the predefined and the dashed line shows the actual temperature profile

## 3.2 Scanning electron microscopy

As the size, amount and distribution of non-metallic inclusions within the weld metal strongly influence its austenite to ferrite transformation, SEM investigations of these inclusions have been conducted. Figure 5 shows various SEM pictures of the 2.25Cr-1Mo-0.25V weld metal sample at different magnifications. Here, the SEM image in Fig. 5a gives an overview of the ferritic lath structure and the distribution of non-metallic inclusions in the weld metal microstructure which protrude from the sample surface due to the etching attack of the surrounding matrix and therefore appear brighter than the matrix. The darker spots are regions on the surface where non-metallic inclusions pulled out during sample preparation or electrolytical polishing. All of the non-metallic inclusions in the SEM-picture exhibit sizes below 1 μm. According to the modified schematic drawing of different non-metallic inclusions in Fig. 1 and the classification implemented by Lee et al. [13], most of the inclusions where type 1 or type 2 inclusions and the type 3 and type 4 inclusions are a minority, see red arrows in Fig. 5a. Inclusions of type 1 and type 2 are assumed to be not suitable for intragranular nucleation of AF and inclusions of type 3 and type 4 can possibly act as nucleation sites for AF laths [13]. It can be seen that very small inclusions with diameters below 0.5 μm are of type 1 or type 2 in most cases. One of the type 4 inclusions which can act as nucleation site for intragranular AF formation is shown at higher magnification. It can be seen that 4 ferrite laths surround the inclusion. Figure 5b again shows a non-metallic inclusion of type 4 at lower and higher magnification. The ferrite laths are oriented star-like around the inclusion and also a small lath grows away from the inclusion next to the bigger laths, see red arrow.

## 3.3 Energy-dispersive X-ray diffraction

Since the chemical composition of the non-metallic inclusions plays an important role relative to their ability to act as a surface for intragranular nucleation, EDX mappings of the inclusions were made. An example of an EDX mapping of a type 4 non-metallic inclusion is shown in Fig. 6. It is a chemical homogeneous oxide consisting of aluminium, silicon and manganese. It is clearly visible that it is depleted in iron.

To obtain better statistics about the nature of the non-metallic inclusions present in the investigated 2.25Cr-1Mo-0.25V SAW weld metal, automated EDX analysis of inclusions ≥ 1 μm was carried out on a 19.5 mm² region in the last weld bead leading to a total number of more than 17,000
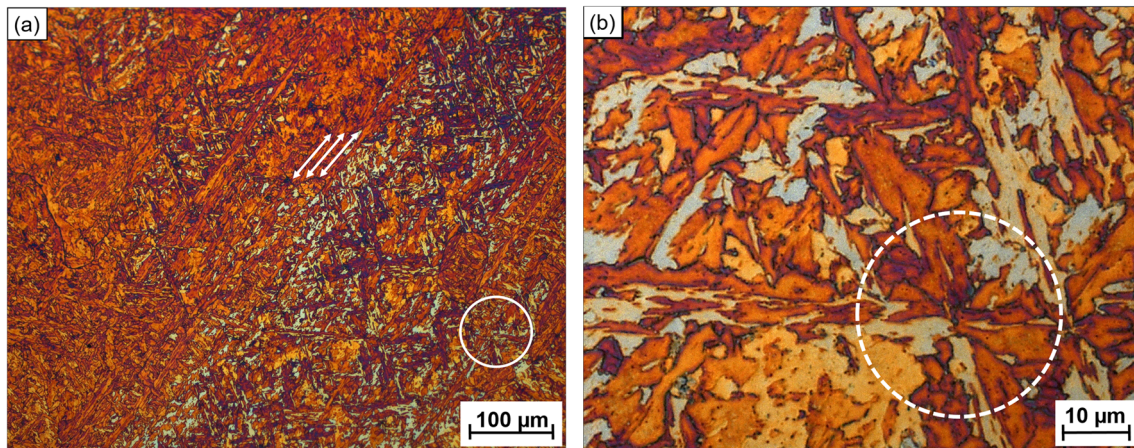
**Fig. 4** OM image of a SAW colour-etched 2.25Cr-1Mo-0.25V weld metal at (**a**) lower magnification and (**b**) higher magnification. The parallel arrows mark an area of parallel lath arrangement and the circles highlight areas of interlocking lath placement and star-like lath arrangement

investigated non-metallic inclusions. The EDX mapping revealed that more than 99% of the non-metallic inclusions were oxides. Furthermore, 96.5% of these oxides were complex aluminium-manganese-silicon oxides like the non-metallic inclusion shown in Fig. 6. All investigated oxides where spherical in shape and regarding the size distribution in Fig. 7, it can be seen that the majority of the complex aluminium-manganese-silicon oxides had a diameter of 1.4 µm leading

to a mean diameter of 1.48 µm. It should be noted that no information about the size distribution of the non-metallic inclusions with diameters below 1 µm is available, as inclusions of this small size are below the detection limit.

The formation of the complex aluminium-manganese-silicon oxide inclusions was not investigated in detail. However, it is assumed that they are already present within the liquid phase of the weld pool during cooling and therefore
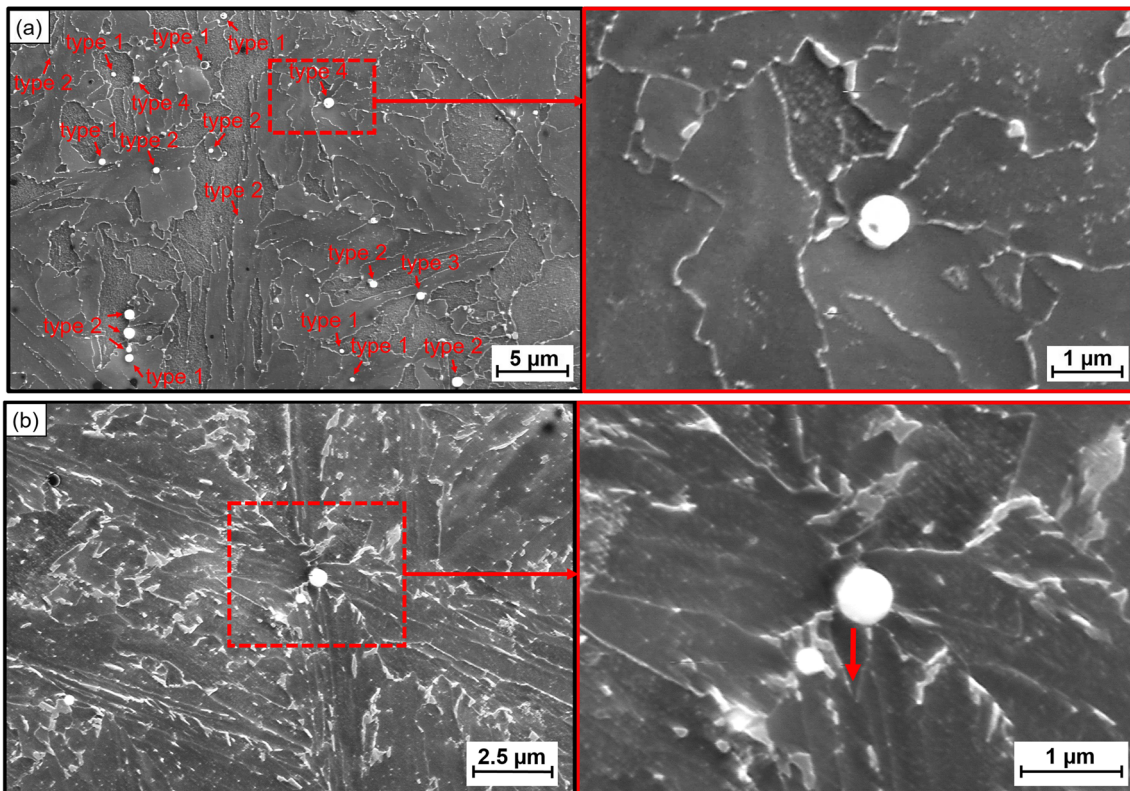


**Fig. 5** SEM images of the electrolytically polished 2.25Cr-1Mo-0.25V weld metal giving (**a**) an overview of the distribution and size of various types of non-metallic inclusions. In the right picture, a type 4 inclusion is shown at higher magnification. **b** The figure shows the star-like arrangement of ferrite laths around an inclusion with low and high magnification. The red arrow marks a small lath growing from the inclusion surface
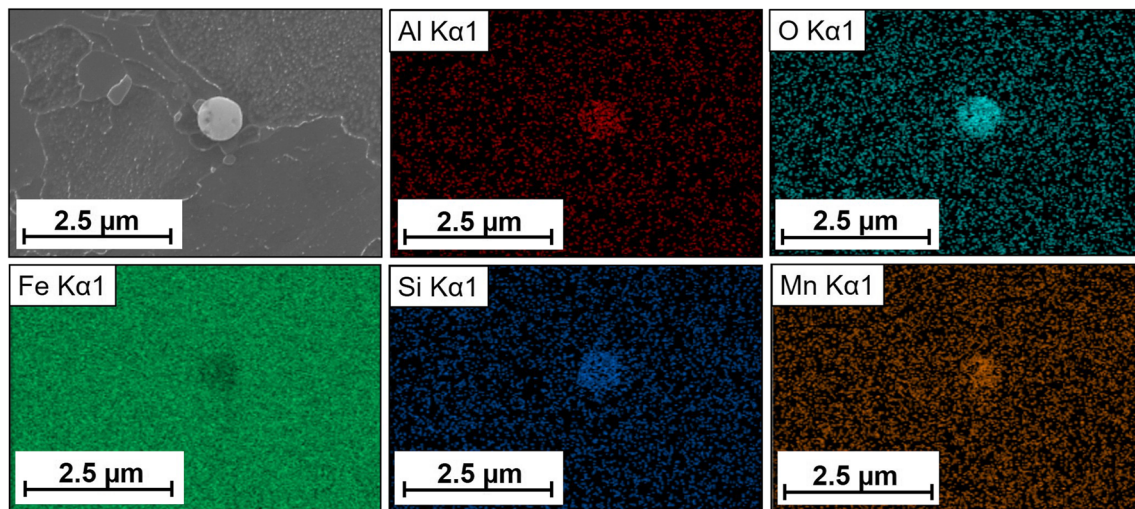
**Fig. 6** SEM pictures of a type 4 non-metallic inclusion with the related EDX results showing that the inclusion is a homogeneous oxide composed of aluminium, silicon and manganese

being able to influence subsequent phase transformations within the weld metals microstructure.

## 3.4 Electron backscatter diffraction

EBSD measurements performed on the electrolytically polished weld metal samples were analysed in terms of lath arrangement, size and shape of prior austenite grains, crystallographic orientations of the ferrite laths within a prior austenite grain and the misorientation angles of ferrite lath boundaries.

Figure 8 shows an inverse pole figure (IPF) map of a region in the last weld bead as has been shown in the overview of the weld metals cross section in Fig. 2. The prior austenite grain
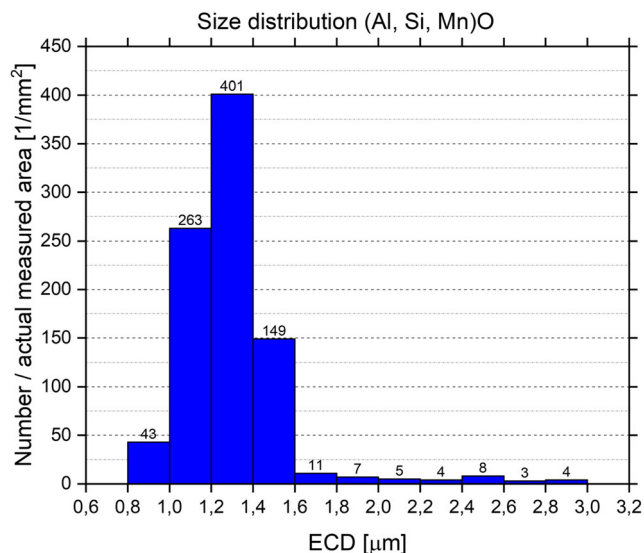


**Fig. 7** Size distribution of the aluminium-manganese-silicon oxides exhibiting diameters above 1 μm measured in a 19.5 mm$^2$ region within the last weld bead of the investigated 2.25Cr-1Mo-0.25V SAW weld metal

boundaries can easily be differentiated as the ferrite laths show different combinations of crystallographic orientations within neighbouring austenite grains. Consequently, it can be seen that the austenite grains are elongated in the direction of solidification and consist of several hundred micrometres in length and several ten micrometres in transverse direction. As pointed out in the OM pictures in Fig. 4a, b), the ferrite laths form parallel structures on the one hand and chaotically aligned features with very different crystallographic orientations on the other hand.

Detail (1), (2) and (3) on the left boarder of Fig. 8 represent regions of classical upper bainite. Whereas in detail (1) a perpendicularly aligned packet of parallel arranged ferrite laths is shown, the laths in the bainitic packet in detail (2) were aligned parallel. In detail (3), large ferrite laths (drawn-through arrows) separate smaller packets of parallel laths (dashed arrows) which lie within a certain angle to the longer separating laths. In between these ordered packets, some regions contain very small laths which do not seem to be in an ordered arrangement (circles). In contrast to these bainitic appearing areas, details (4), (5) and (6) positioned on the right side of Fig. 8 show areas of chaotic lath arrangement with high magnification. The laths in these details exhibit a wide range of crystallographic orientations compared to those shown in detail (1) and (2) where the packets of parallel laths mainly belong to two different crystallographic orientations.

Figure 9 deals with the crystallographic orientations of the ferrite laths within prior austenite grains. In Fig. 9a, a grain map of the investigated region is shown. One can see mainly plate-like ferrite laths which are oriented parallel exhibiting narrow regions of small chaotically arranged ferrite laths in-between. Figure 9b shows the corresponding prior austenite grain structure reconstructed with the program ARPGE by Cayron [40] using Nishyama-Wasserman orientation relationship $((111)_\gamma // (110)_\alpha$ and $[110]_\alpha // [211]_\gamma)$ for the
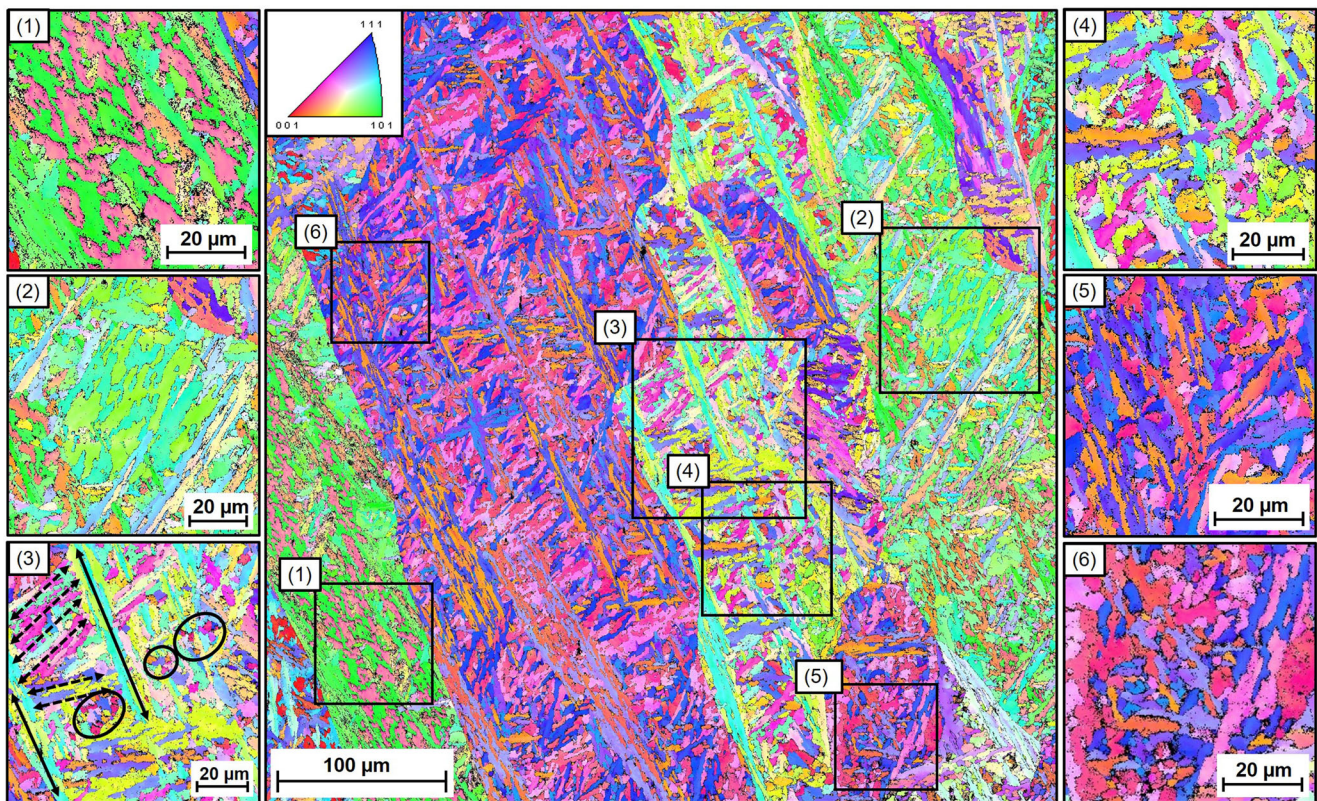
**Fig. 8** IPF map of a region in the last weld bed. Some areas are highlighted using numbered squares and are shown with higher magnifications on the right and left side of the IPF map. The highlights (1), (2) and (3) show areas of parallel arranged ferrite laths forming bainitic packets. The highlights (4), (5) and (6) show a chaotic, interlocking placement of laths exhibiting a variety of crystallographic orientations

recalculation from ferrite to austenite grains. According to A.-F. Gourgues [41], Nishyama-Wasserman orientation relationship is more suitable for bainitic ferrite and intragranular AF than Kurdjumov-Sachs orientation relationship resulting in a higher quality of reconstruction.

It can be seen that the investigated area of the weld metal consists of four prior austenite grains in total. Figure 9c shows an image quality map of the 4 calculated grains. Each of these four prior austenite grains consists of various ferrite laths with different crystallographic orientations. Laths exhibiting similar crystallographic orientations are coloured in shades of red, blue and yellow, respectively. The related (111) pole figures to the 4 austenite grains are illustrated in Fig. 9d. It can be noted that each prior austenite grain consists of ferrite laths contributing to three different crystallographic orientations. The comparison of the (111) pole figures of the four austenite grains investigated in Fig. 9 leads to the suggestion that prior austenite grain number 3 and number 4 actually belong together as they exhibit the same (111) pole figure.

Figure 10a shows the corresponding IPF map and Fig. 10b, the grain boundary map of the same region in the last weld bead shown in Fig. 9. Some sections are highlighted in each image. Highlight (1) shows an area with parallel lath arrangement, whereby the laths forming the packet correspond to two

different crystallographic areas, as can be seen in the IPF map in Fig. 10a. The areas in highlight (2) and highlight (3) differ from the surrounding microstructure as they consist of small irregular arranged laths. In highlight (2), the laths seem to have grown star-like. All the lath boundaries turned out to be high angle boundaries with misorientation angles mostly greater than 40°, whereby a high density of low angle boundaries was found within the ferrite laths, see Fig. 10b.

### 3.5 High-temperature laser confocal microscopy

Figure 11 and Fig. 12 show the process of austenite to ferrite phase transformation. It is evident that in many austenite grains, the transformation starts intragranularly at some inclusions within the austenite grains followed or accompanied by grain boundary nucleation of parallel aligned bainitic ferrite laths. Such intragranular nucleation events at active nonmetallic inclusions are marked with red circles and dashed arrows. Nucleation events occurring directly at the austenite grain boundaries are highlighted with solid line arrows. For all austenite grains presented in Fig. 11 and Fig. 12, the transformation start temperature lies below 500 °C.

The overview in Fig. 11 shows several austenite grains with a size ranging between 40 and 200 μm in diameter. The
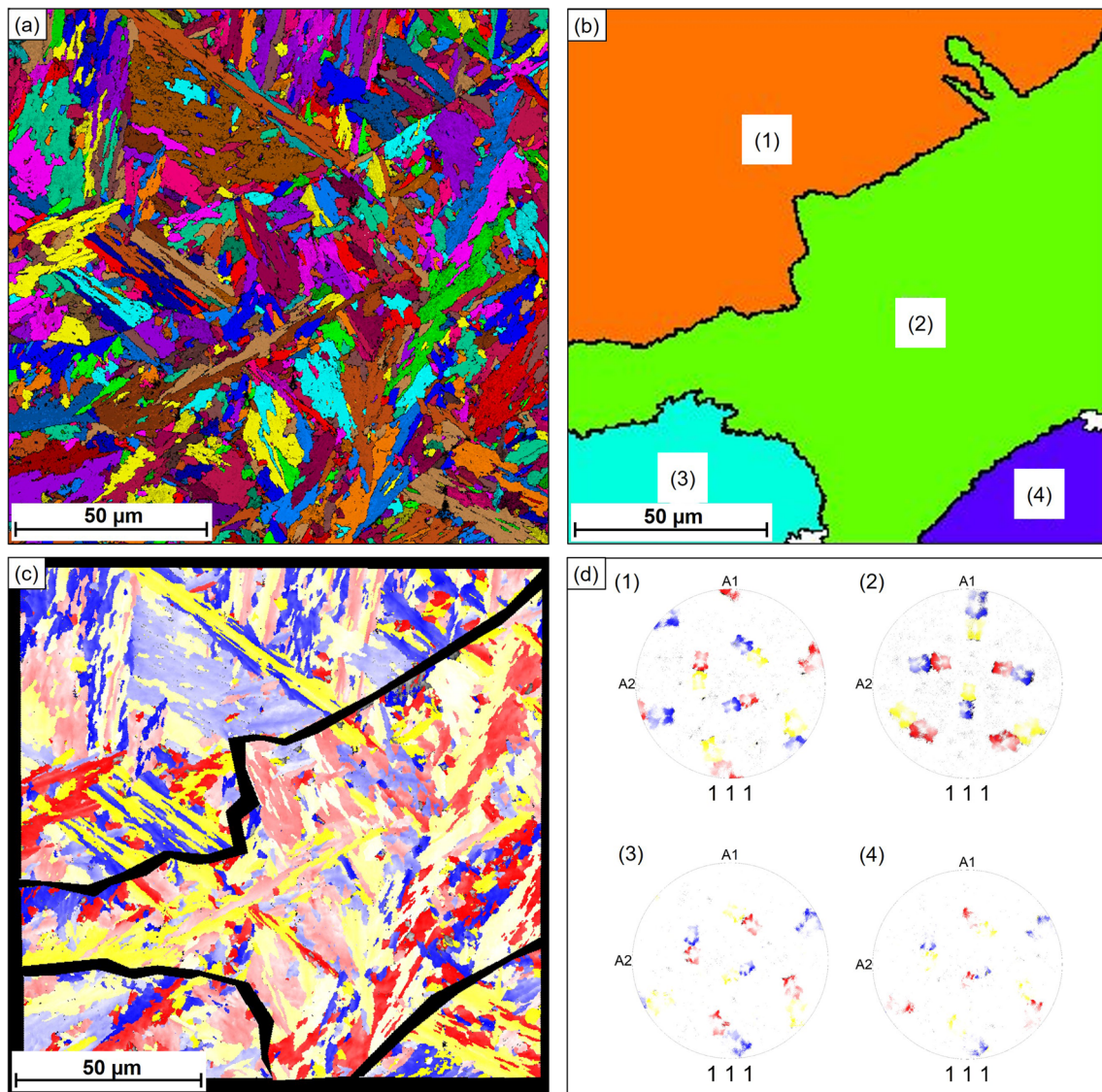
**Fig. 9** Crystallographic investigation of ferrite laths within a parent austenite grain showing (**a**) the grain boundary map with (**b**) the corresponding prior austenite grain map reconstructed using the program ARPGE [40], (**c**) a map of prior austenite grains with crystallographically related ferrite grains dyed in shades of red, blue and yellow respectively and (**d**) the related (111) pole figures

initial austenitic microstructure can be seen in Fig. 11a and the completely transformed bainitic-ferritic microstructure can be seen in Fig. 11f. It is apparent that in some of the austenite grains, the first nucleation events take place within the grain at non-metallic inclusions resulting in laths growing away from the inclusion surfaces. In many cases, just a single lath grows away from the inclusion surface at first, followed by a second one growing in a different direction. An example for two laths nucleated at the same non-metallic inclusion is highlighted in Fig. 11c, see green framed austenite grain. Parallel to the intragranular nucleation of laths, ferrite laths start to grow from the austenite grain boundary as well. These ferrite laths originating from grain boundaries grow in form of parallel packets separating the austenite grain and hence form the basis for further packets of parallel laths, see blue highlighted grain

in Fig. 11e. Beside the nucleation of parallel ferrite laths on an already existing bainitic packet within the austenite grain, also an intragranular nucleation event at an inclusion which acted as a nucleation site for a ferrite lath before (see Fig. 11d) can be noted in the green framed austenite grain in Fig. 11e.

In comparison to Fig. 11 where many smaller austenite grains are visible, Fig. 12 shows the austenite to ferrite transformation of a large austenite grain with more than 150 μm in diameter. Here in Fig. 12a, the initial austenitic microstructure and in Fig. 12b, the austenite to ferrite transformation start can be seen in detail. The transformation starts intragranularly at a non-metallic inclusion within the austenite grain at a temperature of 476 °C. Two ferrite laths originate from the inclusion and grow in different directions. As the temperature decreases further, intragranular nucleation at inclusions takes place accompanied by
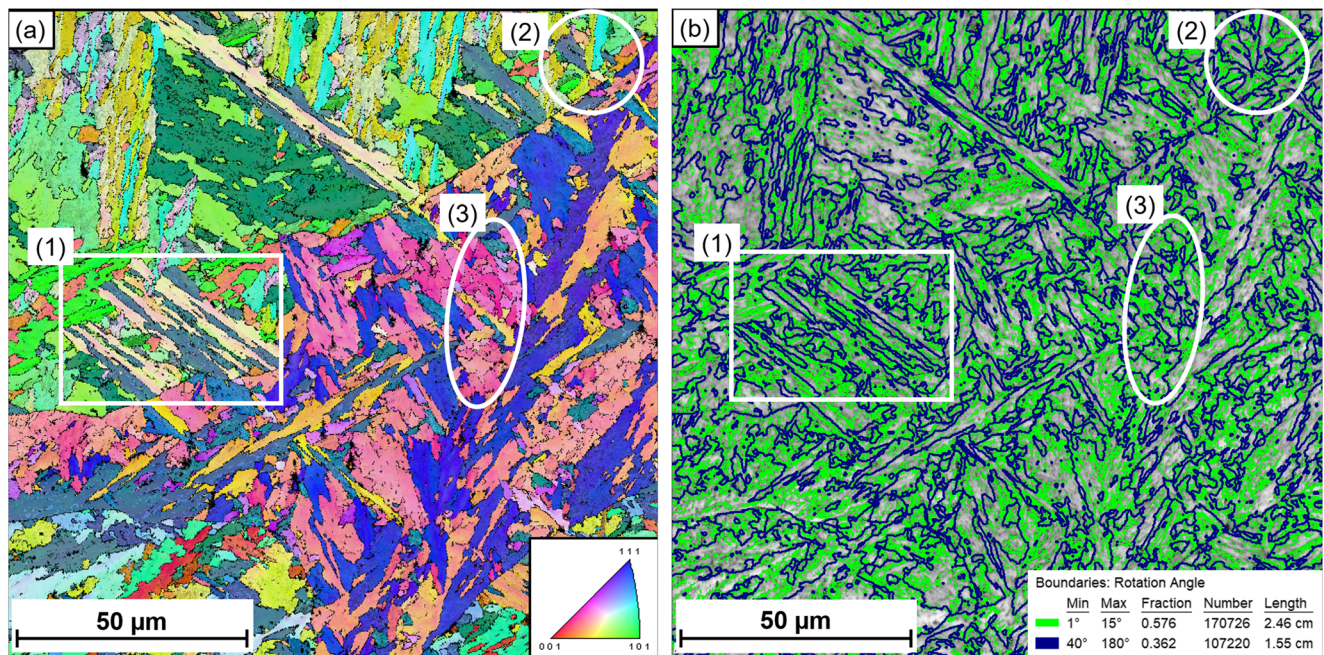
**Fig. 10** **a** IPF map showing the crystallographic orientations of the ferrite laths within the prior austenite grains and **b** grain boundary map exhibiting high angle boundaries with misorientations greater than 40° and a high density of low angle boundaries within the ferrite grains. The highlighted areas mark regions of parallel and chaotic lath arrangement

supplementary grain boundary nucleation, see Fig. 12c to g. In Fig. 12e, many intragranular nucleation events at non-metallic inclusions are visible in the lower regions of the austenite grain. These intragranular nucleated laths subsequently lead to sympathetic nucleation of further ferrite laths, resulting in an interlocking ferritic lath structure which appears chaotic compared to regions of parallel aligned bainitic ferrite laths. In Fig. 12f, a single ferrite lath is highlighted with a red rectangle. It is assumed that this lath originates from an inclusion beneath the surface which is not visible on the specimen surface as another lath grows away from this initial lath in a random direction showing no parallelism to other laths in this area of the austenite grain, see red rectangle in Fig. 12g. Figure 12h shows the final microstructure after the austenite to ferrite transformation was completed. Regions where many intragranular nucleation events took place exhibit an interlocking chaotic lath structure which differs significantly from regions of bainitic ferrite showing parallel alignment of ferrite laths, see labelling in Fig. 12h.

## 4 Discussion

The aim of this paper was to clarify if AF is a microstructural constituent in 2.25Cr-1Mo-0.25V SAW weld metal. Furthermore, it was evaluated through comparison with literature findings if given circumstances such as prior austenite grain size, non-metallic inclusions and the chemical composition of the weld metal are beneficial for the formation of this intragranularly nucleated microstructure constituent.

The investigation of the non-metallic inclusions revealed that the majority of the inclusions were type 1 and type 2 inclusions which cannot act as nucleation sites according to literature [13]. In most cases, smaller inclusions with diameters below 0.5 μm were of type 1 and type 2. However, beside these inert inclusions, also, some type 3 and type 4 inclusions where found exhibiting several ferrite laths originating from their interface. Even though it cannot be determined whether the ferrite laths grew from the inclusion interface during austenite to ferrite transformation or whether the ferrite laths randomly grew around the inclusion, small ferrite laths directly going away from the inclusion interface like it can be seen in Fig. 5b and Fig. 6 indicate that the inclusion played a role in the nucleation process. The EDX analysis revealed that the inclusions with sizes greater than 1 μm were complex oxides composed of aluminium, silicon and manganese. Furthermore, the inclusions where chemically homogeneous exhibiting only slight variations of the major elements from inclusion to inclusion and no chemical segregations such as shells were found in the course of EDX analysis. Therefore, it is expected that the major elements manganese, aluminium and silicon were combined with oxygen leading to a complex single phase oxide within the ternary system $MnO$-$Al_2O_3$-$SiO_2$. So, the type 4 oxide shown in Fig. 6 is in good agreement with the total of the non-metallic inclusions exhibiting diameters greater than 1 μm present in the investigated 2.25Cr-1Mo-0.25V weld metal. Sarma et al. [14] summarized that among the oxide inclusions, simple inclusions like $Al_2O_3$ are not considered being an effective nuclent. However,
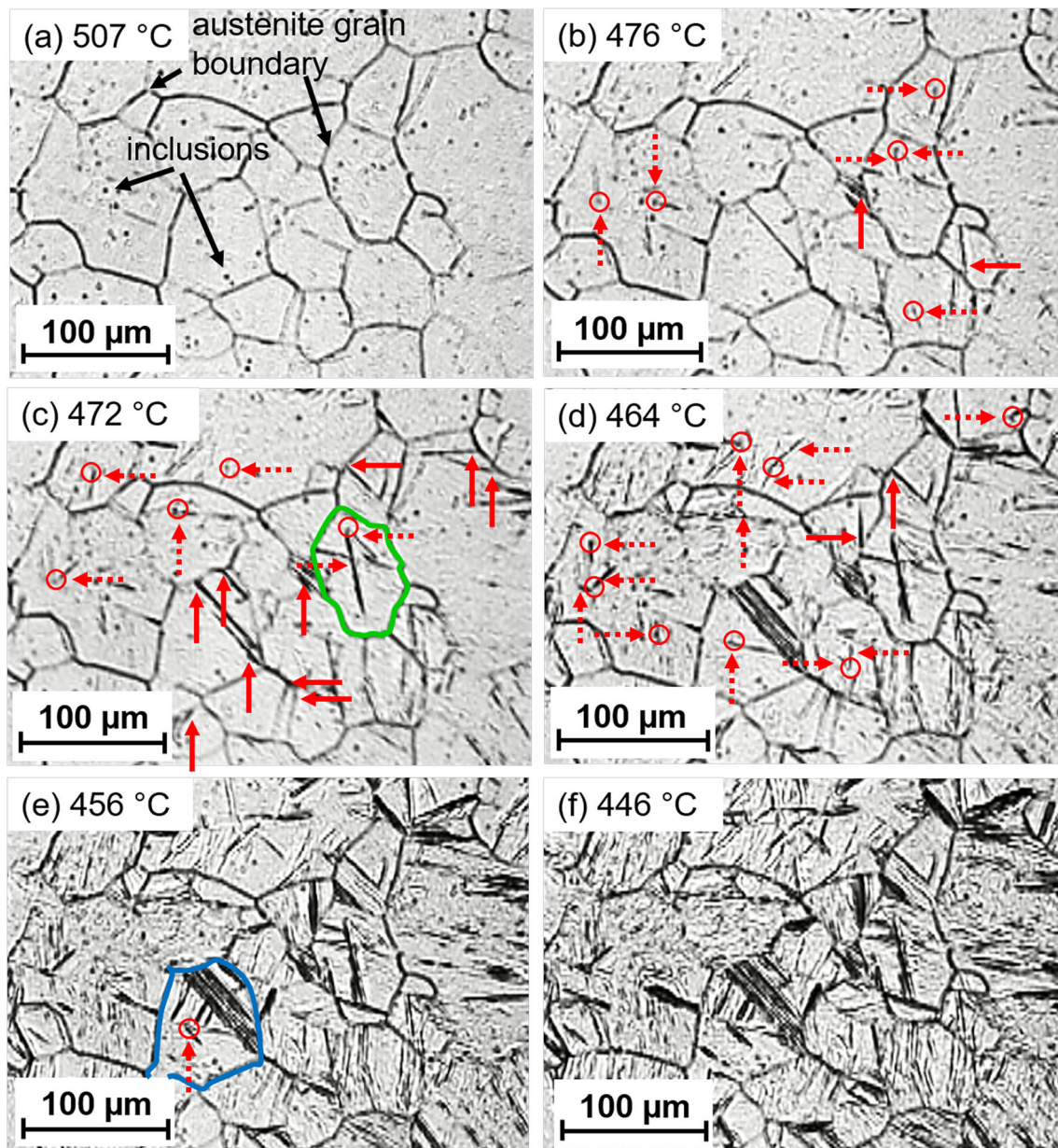
**Fig. 11** HT-LSCM pictures of the in situ observation of the morphological development of the austenite to ferrite phase transformation process at different temperatures (**a**–**f**). Circles and dashed arrows mark intragranular nucleation events of ferrite laths on the surface of non-metallic inclusions and continuous lined arrows mark nucleation of ferrite laths at austenite grain boundaries

Al₂O₃ in combination with MnO such as galaxite spinel is able to act as nucleus for AF. Ti₂O₃ showed a similar behaviour like Al₂O₃. Ti₂O₃ is ineffective as nucleus except the steel contains manganese. Only TiO can act as nuclei for AF itself without containing additional MnO. Among the more complex inclusions, galaxite-type inclusions such as aluminium-manganese silicates which can form in manganese bearing steels being deoxidized using aluminium and silicon work as effective nucleus for AF. In contrast to these, aluminium-manganese silicates, calcium-aluminate and CaO-Al₂O₃-SiO₂ inclusions as well as MgO-Al₂O₃ spinel-type inclusions, do not favour the nucleation of AF [7, 14, 42]. Also, Zhang et al. concluded from previous studies that complex oxide inclusions like Al₂O₃-MnO-SiO₂ and TiO-MnO-SiO₂ are able to act as intragranular nucleation site for AF laths [24]. Furthermore, Dowling et al. [43] concluded that high melting phases such as TiO, Al₂O₃-MnO, SiO₂, MnS and Al₂O₃ which exhibit high surface energies are more likely to act as inert substrate for intragranular AF nucleation. This is because high energy interfaces exist between these types of non-metallic inclusions and the surrounding matrix leading to a low energy barrier for ferrite nucleation according to the classical theory of heterogeneous nucleation. Furthermore, multiphase inclusions provide a higher probability of having

**Fig. 12** HT-LSCM pictures of the in situ observation of the morphological development of the austenite to ferrite phase transformation process in one large austenite grain at different temperatures (**a**–**h**). Circles and dashed arrows mark intragranular nucleation events of ferrite laths and continuous lined arrows mark nucleation of laths at austenite grain boundaries
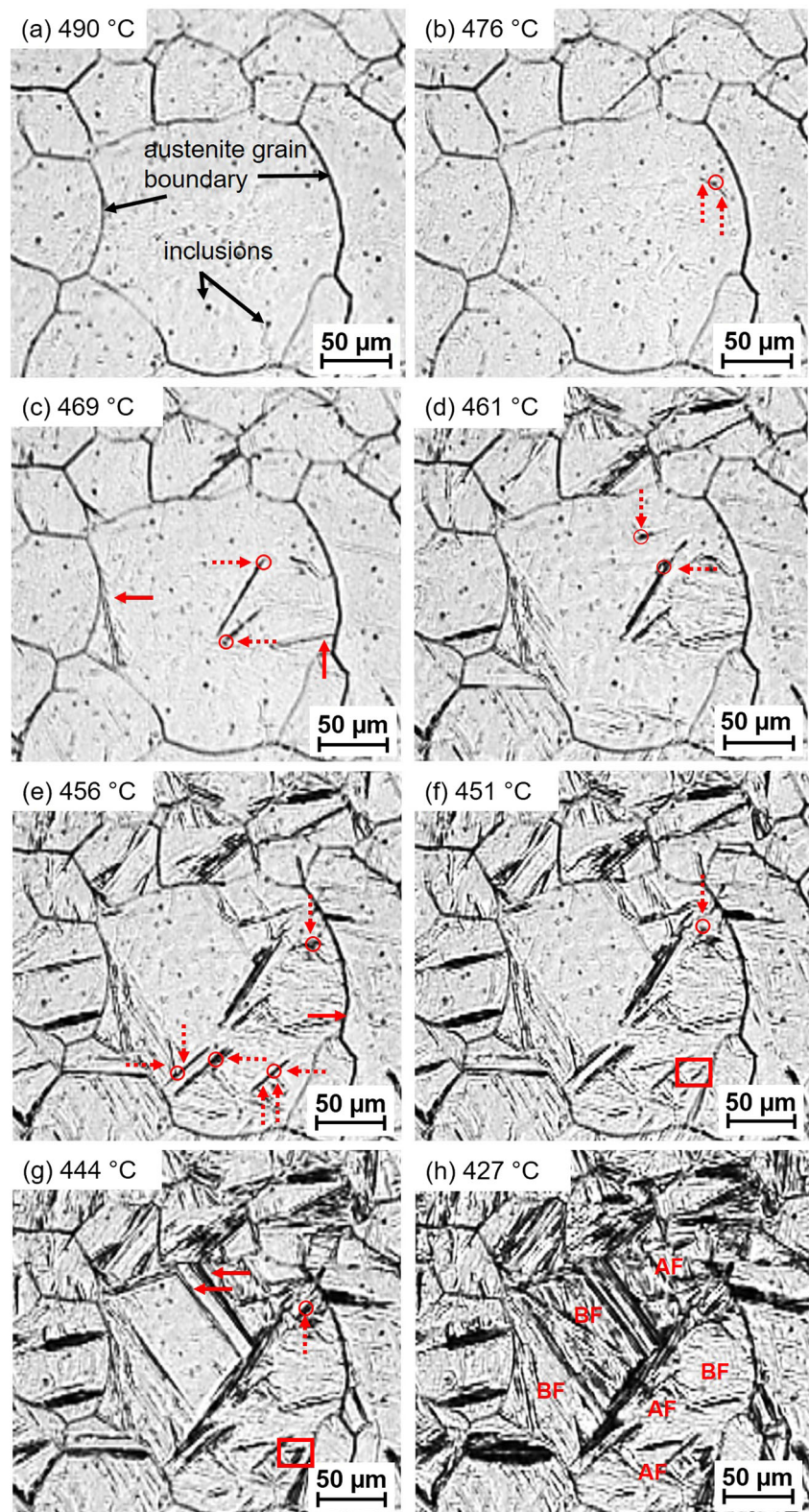


multiple regions of high surface energy [43]. In addition, the 2.25Cr-1Mo-0.25V weld metals oxygen content of 220 ppm lies within the beneficial range for AF formation which is 150 to 300 ppm according to Barbaro et al. [18]. The EDX mapping of the non-metallic inclusions revealed that the mean diameter of the investigated inclusions with diameters ≥ 1 μm was 1.48 μm. Regarding literature [13], such large non-metallic inclusions exhibit a higher potential of being possible

intragranular nucleation sites as with increasing size the energy barrier for nucleation lowers rapidly. To summarize, the EDX mapping clearly showed that the larger inclusions exhibiting diameters above 1 μm are mainly complex single phase Manganese-Aluminium-Silicon oxides which are known to be favourable intragranular nucleation sites regarding literature findings [7, 13, 14, 24, 42, 43].

The OM images show that beside regions of parallel ferrite laths which form bainitic packets, other areas consist of chaotically aligned laths which sometimes appear star-like.

Beside the microstructure investigation by means of OM and SEM, also the crystallographic investigation by means of EBSD indicated that AF might be a microstructure constituent in 2.25Cr-1Mo-0.25V SAW weld metal. The interlocking ferrite lath arrangement and the partially very small lath size clearly differs from the regions of parallel lath arrangement. Nonetheless, it is difficult to distinguish whether these chaotically arranged laths nucleated intragranularly at non-metallic inclusions or, whether they are small packets of parallel ferrite laths, which intersect perpendicularly. Depending on the angle between small bainitic packets of ferrite laths and the specimen surface, the lath arrangement can appear more or less ordered during microstructure investigation. However, in such regions of disorderly aligned ferrite laths, the ferrite laths exhibit numerous crystallographic orientations, which is again characteristic for this kind of microstructure constituent. The investigated austenite grains exhibit three texture components of ferrite laths per prior austenite grain and the ferrite laths exhibit high angle boundaries with misorientation levels greater than 40° and a high density of low angle boundaries in between which is applicable for both bainitic ferrite and AF as stated in literature [41]. As AF and bainitic ferrite exhibit no significant differences regarding their crystallography except the varying lath arrangement and the different distribution of crystallographic orientations, the investigation of grain boundary misorientations and texture components of ferrite laths within the prior austenite grains were not sufficient for a definitive determination of the weld metals microstructure constituents.

Regarding the results of the OM, SEM, EDX and EBSD investigation of the fully transformed weld metal microstructure, it was not possible to draw an unambiguous conclusion concerning the presence of AF in 2.25Cr-1Mo-0.25V SAW weld metal as the main difference between this microstructure constituent and classical bainitic ferrite which both form in the bainite temperature region is its nucleation mechanism.

Therefore, in-situ methods with which the austenite to ferrite transformation can be directly investigated are more suitable to draw a reliable distinction. By means of HT-LSCM, the austenite to ferrite transformation was investigated in-situ, which made it possible to retrace the formation of single ferrite laths and packets of parallel laths. Heating the weld metal specimen in the austenite phase field does not influence the

nature of non-metallic inclusions which makes the investigated transformation comparable to the real welding process. However, the limited cooling rate of the HT-LSCM system has to be taken into account. The transformation steps captured in Fig. 11 and Fig. 12 demonstrate that despite the comparably high chromium and molybdenum contents, intragranular nucleation events took place at non-metallic inclusions during cooling. In many cases, two laths grew from one non-metallic inclusion exhibiting different orientations which did not correspond to the surrounding laths leading to the assumption that the ferrite laths directly nucleated on the interface of the non-metallic inclusion and did not grow from beneath the specimen's surface. The temperature of the austenite to ferrite transformation start lies below 500 °C for the investigated areas shown in Fig. 11 and Fig. 12 and thus is in good agreement with literature which states a temperature range of 650 to 440 °C for AF nucleation [14]. The comparably low transformation start temperature may correlate with the weld metals high manganese content of 1.14 wt.% as increasing levels of manganese are known to depress the austenite to ferrite transformation temperature [10].

In conclusion, the in-situ HT-LSCM investigation revealed that the formation of intragranularly nucleated AF is taking place in 2.25Cr-1Mo-0.25V SAW weld metal. Nevertheless, bainitic ferrite nucleated at austenite grain boundaries makes up the majority of the microstructure and AF only appears in small amounts in between. This is in accordance with the assumption of Babu et al. [15] who investigated metal arc welds with a chromium content of 1.59 wt.%. Fe-Cr-Mo-C weldments tend to have high levels of bainitic ferrite due to the suppression of allotriomorphic ferrite leading to austenite grain boundaries which are free for ferrite nucleation and in further consequence to a reduction of the quantity of AF [15]. Nonetheless, the combination of large austenite grains with a high density of complex spherical aluminium-manganese-silicon oxides in 2.25Cr-1Mo-0.25V SAW weld metal seems to be sufficient for the formation of AF. Further investigations have to be done whether an occupation of the austenite grain boundaries through segregation of soluble elements like, e.g. boron retards the nucleation at grain boundaries in a sufficient matter and thus is able to favour intragranular nucleation leading to higher amounts of AF in 2.25Cr-1Mo-0.25V weld metal.

# 5 Conclusions

The microstructure of 2.25Cr-1Mo-0.25 V SAW weld metal was examined regarding the existence of intragranularly nucleated AF using OM, SEM, EDX, EBSD and XRD as well as in situ HT-LSCM. Based on the investigations carried out, following conclusions can be drawn:

- OM, SEM and EBSD are not sufficient methods to distinguish between the different microstructural constituents formed in the bainite temperature region.
- A clear assertion whether the investigated 2.25Cr-1Mo-0.25V weld metal contains AF could be drawn only by investigating the austenite to ferrite transformation by means of in situ methods such as HT-LSCM.
- The crystallographic investigation using EBSD revealed that the ferrite laths within the prior austenite grains consisted of three texture components and the ferrite lath boundaries where high angle boundaries with misorientations greater than 40° which is typical for both baintic ferrite and AF.
- The weld metal exhibits a high density of non-metallic inclusions which are complex homogeneous aluminium-silicon-manganese oxides with a spherical shape.
- Despite the relatively high chromium and molybdenum content which is typically not favourable for the formation of AF, intragranular nucleation of ferrite laths at non-metallic inclusions was detected via in-situ HT-LSCM during austenite to ferrite transformation.
- To summarize, the microstructure of 2.25Cr-1Mo-0.25V SAW weld metal mainly consists of bainitic ferrite nucleated at austenite grain boundaries with narrow regions of AF nucleated at the interface of non-metallic inclusions.

# References

1. Hucińska J (2003) Advanced vanadium modified steels for high pressure hydrogen reactors. Adv Mater Sci 4(2):21–27
2. Detemple I, Hanus F, Luxenburger G (1999) Advanced steels for hydrogen reactors. Hydrocarb Eng 4:1–8
3. Chovet C, Schmitt J-P (2011) Additional recommendations for welding Cr-Mo-V steels for petrochemical applications. Weld World 55(11–12):31–38. https://doi.org/10.1007/BF03321540
4. Dhooge A, Vinckier A (1987) Reheat cracking—a review of recent studies. International Journal of Pressure Vessels and Piping. International Journal of Pressure Vessels and Piping 27(4):239–269. doi:https://doi.org/10.1016/0308-0161(87)90012-3
5. API Recommended Practice 941 (2016) Steels for hydrogen service at elevated temperatures and pressures in petroleum refineries and petrochemical plants, 8. Aufl. API Publishing Services
6. Nelson GA Hydrogenation plant steels. In: Beachem, C. D, American Society for Metals, Metals Park, OH, S 377–394
7. Thewlis G (1994) Transformation kinetics of ferrous weld metals. Mater Sci Technol 10(2):110–125. https://doi.org/10.1179/mst.1994.10.2.110
8. Yang JR, Bhadeshia HKDH (1991) Acicular ferrite transformation in alloy-steel weld metals. J Mater Sci 26(3):839–845. https://doi.org/10.1007/BF00588325
9. Byun J-S, Shim J-H, Suh J-Y, Oh Y-J, Cho YW, Shim J-D, Lee DN (2001) Inoculated acicular ferrite microstructure and mechanical properties. Mater Sci Eng A 319-321:326–331. https://doi.org/10.1016/S0921-5093(00)02014-1
10. Farrar RA, Harrison PL (1987) Acicular ferrite in carbon-manganese weld metals: an overview. J Mater Sci 22(11):3812–3820. https://doi.org/10.1007/BF01133327
11. Zhang D, Terasaki H, Y-i K (2010) In situ observation of the formation of intragranular acicular ferrite at non-metallic inclusions in C–Mn steel. Acta Mater 58(4):1369–1378. https://doi.org/10.1016/j.actamat.2009.10.043
12. Terasaki H, Komizo Y (2006) In situ observation of morphological development for acicular ferrite in weld metal. Sci Technol Weld Join 11(5):561–566. https://doi.org/10.1179/174329306X149795
13. Lee T-K, Kim HJ, Kang BY, Hwang SK (2000) Effect of inclusion size on the nucleation of acicular ferrite in welds. ISIJ Int 40(12):1260–1268. https://doi.org/10.2355/isijinternational.40.1260
14. Sarma DS, Karasev AV, Jönsson PG (2009) On the role of non-metallic inclusions in the nucleation of acicular ferrite in steels. ISIJ Int 49(7):1063–1074. https://doi.org/10.2355/isijinternational.49.1063
15. Babu SS, Bhadeshia HKDH (1990) Transition from bainite to acicular ferrite in reheated Fe–Cr–C weld deposits. Mater Sci Technol 6(10):1005–1020. https://doi.org/10.1179/mst.1990.6.10.1005
16. Abson DJ, Pargeter RJ (1986) Factors influencing as-deposited strength, microstructure, and toughness of manual metal arc welds suitable for C-Mn steel fabrications. Int Met Rev 31(1):141–196. https://doi.org/10.1179/imtr.1986.31.1.141
17. Harrison PL, Farrar RA (1981) Influence of oxygen-rich inclusions on the $\gamma \rightarrow \alpha$ phase transformation in high-strength low-alloy (HSLA) steel weld metals. J Mater Sci 16(8):2218–2226. https://doi.org/10.1007/BF00542384
18. Barbaro FJ, Krauklis P, Easterling KE (1989) Formation of acicular ferrite at oxide particles in steels. Mater Sci Technol 5(11):1057–1068. https://doi.org/10.1179/mst.1989.5.11.1057
19. Mortimer DA, Nicholas MG (1976) Surface and grain-boundary energies of AISI 316 stainless steel in the presence of boron. Met Sci 10(9):326–332. https://doi.org/10.1179/msc.1976.10.9.326
20. Jun HJ, Kang JS, Seo DH, Kang KB, Park CG (2006) Effects of deformation and boron on microstructure and continuous cooling transformation in low carbon HSLA steels. Mater Sci Eng A 422(1–2):157–162. https://doi.org/10.1016/j.msea.2005.05.008
21. Zhang D, Shintaku Y, Suzuki S, Komizo YI (2012) In situ observation of phase transformation in low-carbon, boron-treated steels. Metall Mater Trans A 43(2):447–458. https://doi.org/10.1007/s11661-011-0892-8
22. Lee HW, Kim YH, Lee SH, Lee KH, Park JU, Sung JH (2007) Effect of boron contents on weldability in high strength steel. J Mech Sci Technol 21(5):771–777. https://doi.org/10.1007/BF02916355
23. Karasev AV, Suito H (2008) Effects of oxide particles and solute elements on austenite grain growth in Fe–0.05mass%C and Fe–

10mass%Ni alloys. ISIJ Int 48(5):658–666. https://doi.org/10.2355/isijinternational.48.658

24. Zhang Z, Farrar RA (1996) Role of non-metallic inclusions in formation of acicular ferrite in low alloy weld metals. Mater Sci Technol 12(3):237–260. https://doi.org/10.1179/mst.1996.12.3.237

25. Zhang D, Shintaku Y, Suzuki S, Y-i K (2012) Effect of cooling rate on phase transformation in the low-carbon boron-treated steel. J Mater Sci 47(14):5524–5528. https://doi.org/10.1007/s10853-012-6444-9

26. Bhaduri AK, Rai SK, Gill TPS, Sujith S, Jayakumar T (2001) Evaluation of repair welding procedures for 2.25Cr–1Mo and 9Cr–1Mo steel welds. Sci Technol Weld Join 6(2):89–93. https://doi.org/10.1179/136217101101538587

27. Clerge M, Boucher C, Pillot S, Balladon P, Bourges PH, Bertoni A (2005) Optimisation of intermediate heat treatments and stress relief of CrMoV steels. Weld Int 19(11):888–893. https://doi.org/10.1533/wint.2005.3495

28. Ichikawa K, Horii Y, Sueda A, Kobayashi J (1995) Thoughness and creep strength of modified 2.25Cr-1Mo steel weld metal. Weld J-Incl Weld Res Suppl 74(7):230–238

29. Lausch T, Kannengiesser T, Schmitz-Niederau M (2013) Multi-axial load analysis of thick-walled component welds made of 13CrMoV9-10. J Mater Process Technol 213(7):1234–1240. https://doi.org/10.1016/j.jmatprotec.2013.01.008

30. Pereira PAS, Franco CSG, Guerra Filho JLM, dos Santos DS (2015) Hydrogen effects on the microstructure of a 2.25Cr–1Mo–0.25 V steel welded joint. Int J Hydrog Energy 40(47):17136–17143. https://doi.org/10.1016/j.ijhydene.2015.07.095

31. Wang CY, Fu RD, Zhou WH, Zhang WH, Zheng YZ (2006) Effect of reheating processes on grain boundary heritance for 2.25Cr–1Mo–0.25V steel. Mater Sci Eng A 438-440:1135–1138. https://doi.org/10.1016/j.msea.2006.02.164

32. Lausch T, Kannengießer T (2015) Zum Einfluss der Wärmeführung auf die Rissbildung beim Spannungsarmglühen dickwandiger Bauteile aus 13CrMoV9–10. Dissertation, Otto-von-Guericke-University Magdeburg

33. Yongtao Z, Haibo H, Lede M, Hanqian Z, Jinfu L (2009) Quantitative carbide analysis using the Rietveld method for 2.25Cr–1Mo–0.25V steel. Mater Charact 60(9):953–956. https://doi.org/10.1016/j.matchar.2009.03.009

34. Yongtao Z, Lede M, Hanqian Z, Jinfu L (2009) Evolution behavior of carbides in 2.25 Cr-1Mo-0.25 V steel. Mater Trans 50(11):2507–2511. https://doi.org/10.1016/j.matchar.2009.03.009

35. Taniguchi G, Yamashita K, Otsu M, Nako H, Sakata M (2015) A study on the development of creep rupture and temper embrittlement properties in 21/4Cr-1Mo-V steel weld metal. Weld World 59(6):785–796. https://doi.org/10.1007/s40194-015-0252-1

36. Kayali ES, Corbett JM, Kerr HW (1983) Observations on inclusions and acicular ferrite nucleation in submerged arc HSLA welds. J Mater Sci Lett 2(3):123–128. https://doi.org/10.1007/BF00722228

37. Loder D, Michelic SK, Bernhard C (2016) Systematische Untersuchung der Azikularferritbildung in Stählen. BHM Berg- und Hüttenmännische Monatshefte 161(7):315–320. https://doi.org/10.1007/s00501-016-0509-z

38. Loder D, Mayerhofer A, Michelic S, Bernhard C, Dippenaar R (2014) In situ observation of acicular ferrite formation using HT-LSCM possibilities, challenges and influencing factors. Proceedings Materials Science and Technology (MS&T) Conference, Pittsburgh, Pennsylvania, USA. ASM International, S 469–476

39. Michelic SK, Loder D, Arth G, Bernhard C (2014) Experimental study on the formation of non-metallic inclusions acting as nuclei for acicular ferrite in HSLA steels through specific deoxidation practice and defined cooling conditions. Mater Sci Forum 783-786:1079–1084. https://doi.org/10.4028/www.scientific.net/MSF.783-786.1079

40. Cayron C (2007) ARPGE: a computer program to automatically reconstruct the parent grains from electron backscatter diffraction data. J Appl Crystallogr 40(Pt 6):1183–1188. https://doi.org/10.1107/S0021889807048777

41. Gourgues A-F, Flower HM, Lindley TC (2000) Electron backscattering diffraction study of acicular ferrite, bainite, and martensite steel microstructures. Mater Sci Technol 16(1):26–40. https://doi.org/10.1179/026708300773002636

42. Mills AR, Thewlis G, Whiteman JA (1987) Nature of inclusions in steel weld metals and their influence on formation of acicular ferrite. Mater Sci Technol 3(12):1051–1061. https://doi.org/10.1179/026708387790329333

43. Dowling JM, Corbett JM, Kerr HW (1986) Inclusion phases and the nucleation of acicular ferrite in submerged arc welds in high strength low alloy steels. Metall Trans A 17(9):1611–1623. https://doi.org/10.1007/BF02650098